Imaging Atomically Thin Semiconductors Beneath Dielectrics via Deep Ultraviolet Photoemission Electron Microscopy

Morgann Berg,[1,2] Fangze Liu,[3] Sean Smith,[1] R. Guild Copeland,[1] Calvin K. Chan,[1] Aditya D. Mohite,[4] Thomas E. Beechem,[1] and Taisuke Ohta[1,2,*]

[1] *Sandia National Laboratories, Albuquerque, New Mexico 87185, USA*
[2] *Center for Integrated Nanotechnologies, Albuquerque, New Mexico 87185, USA*
[3] *Los Alamos National Laboratory, Los Alamos, New Mexico 87545, USA*
[4] *Department of Chemical and Biomolecular Engineering, Rice University, Houston, Texas 77005, USA*

(Received 19 November 2018; revised manuscript received 20 November 2019; published 31 December 2019)

Imaging of fabricated nanostructures or nanomaterials covered by dielectrics is highly sought after for diagnostics of optoelectronics components. We show imaging of atomically thin MoS_2 flakes grown on SiO_2-covered Si substrates and buried beneath HfO_2 overlayers up to 120 nm in thickness using photoemission electron microscopy with deep-UV photoexcitation. Comparison of photoemission yield (PEY) to modeled optical absorption evinced the formation of optical standing waves in the dielectric stacks (i.e., cavity resonances of HfO_2 and SiO_2 layers on Si). The presence of atomically thin MoS_2 flakes modifies the optical properties of the dielectric stack locally. Accordingly, the cavity resonance condition varies between the sample locations over buried MoS_2 and surrounding areas, resulting in image contrast with submicron lateral resolution. This subsurface sensitivity underscores the role of optical effects in photoemission imaging with low-energy photons. This approach can be extended to nondestructive imaging of buried interfaces and subsurface features needed for analysis of microelectronic circuits and nanomaterial integration into optoelectronic devices.

DOI: 10.1103/PhysRevApplied.12.064064

I. INTRODUCTION

From sonograms to geological surveys, scientists and engineers have searched for accurate and reliable approaches for inspecting internal or “buried” structures nondestructively. For micro and nanoelectronic devices, the challenge has been to achieve the microscopy of buried interfaces and subsurface features, which are often encapsulated within dielectric or insulating films [1,2]. To that end, numerous microscopy techniques have been applied, including optical microscopy [1], imaging ellipsometry [3], scanning and transmission electron microscopies [4–9], and, more recently, scanning probe microscopy [2,10–12], x-ray microscopy [13,14], and photoemission electron microscopy (PEEM) [15,16]. There are three criteria by which successful internal imaging is gauged: spatial resolution down to the nanometer scale, depth sensitivity, and nondestructiveness. Thus far, satisfying all three requirements simultaneously remains elusive.

Of these techniques, PEEM remains promising due to its high depth sensitivity [17] via two known characteristics of photoemission processes: (1) optical standing waves typically formed when using medium- to high-energy photons (x rays) [18–22], and (2) longer photoelectron mean free paths achievable with photoexcitation using high- or very low-energy photons as opposed to medium-energy photons (we specify the photon’s energy range in Ref. [23]) [24–28]. Both approaches can stimulate the photoelectron emission from subsurface regions of the sample. Due to sample charging, dielectrics are excluded from the use of medium- to high-energy photons in photoemission measurement in general. To allow for imaging of samples covered with dielectrics with enhanced depth sensitivity [29,30], we therefore sought to exploit the PEEM imaging with low-energy photons, which can establish optical standing waves [31,32] or generate low-kinetic-energy photoelectrons with anticipated longer mean free paths [7,33]. In this work, we demonstrate subsurface imaging based on PEEM using deep-UV excitation. The optical standing waves formed by deep-UV photons have enabled imaging of atomically thin MoS_2 flakes beneath HfO_2 films up to a 120 nm thick. This sample structure emulates the architecture of general electronics components, in which electrically active layers are buried under passivating dielectrics. We further confirmed imaging subsurface features buried beneath two other oxides—Al_2O_3 and SiO_2. Thus, this approach is viable for subsurface imaging beneath common dielectrics used in microelectronics.

*tohta@sandia.gov

 © 2019 American Physical Society

II. RESULTS

A. Subsurface imaging and photon wavelength-dependent image contrast

Using PEEM with low-energy photons, we image atomically thin MoS_2 flakes covered with varying thicknesses of HfO_2 overlayers as shown in Figs. 1(a)–1(j). We choose HfO_2 overlayers because HfO_2 is commonly used in micro and nanoelectronics owing to its high dielectric constant and it has a relatively high refractive index in the UV spectrum. Layers of MoS_2 are only several-atoms thick (each MoS_2 monolayer is three-atoms thick), making detection of buried MoS_2 layers an excellent test of subsurface sensitivity. Atomically thin MoS_2 flakes (mostly monolayer specimens, with some multilayer regions near the center of the flakes) are grown on Si wafers covered with 100-nm-thick SiO_2 [34]. We then cover the entire sample surface with HfO_2 overlayers via atomic layer deposition (ALD) [35–37]. Thus, SiO_2 and HfO_2 films encapsulate MoS_2 flakes, as illustrated in Figs. 1(k) and 1(l).

Despite being buried, MoS_2 flakes, with their characteristic triangular shape, are visible through the HfO_2 overlayers, ranging in thickness from 0 nm to over 100 nm [37]. Figures 1(a)–1(d) show clear image contrast between the buried MoS_2 and surrounding areas. In addition, the image contrast changes as a function of the photoexcitation wavelength. Figures 1(e)–1(j) show one such example of the wavelength dependence for the 21-nm-thick HfO_2 film [38]. Raman measurement (not shown) confirmed that the small dots near the periphery of MoS_2 flakes are smaller crystallites of MoS_2. We do not encounter sample charging within our detection limit except for the thickest 103-nm-thick HfO_2 overlayer, and only when examined using photons with wavelength below $\lambda = 195$ nm. We suppose that the minimal conductivity of dielectrics (presumably due to defects) is still high enough to replenish the relatively small number of electrons lost during photoemission, when excited by the comparatively low-energy, low-flux photons of deep-UV PEEM. The results highlighted in Fig. 1 are similar to photoemission experiments carried out on conductive samples using hard x rays (i.e., high-energy photons) [28,39], whereas in our case we realized subsurface imaging through insulating dielectrics with deep-UV photons. The notably large depth sensitivity to buried structures is the key outcome of this work.

B. Photoemission yield and optical absorption modeling

The large depth sensitivity as well as the wavelength-dependent image contrast emerges as a consequence of optical standing waves, which form in the dielectric stacks

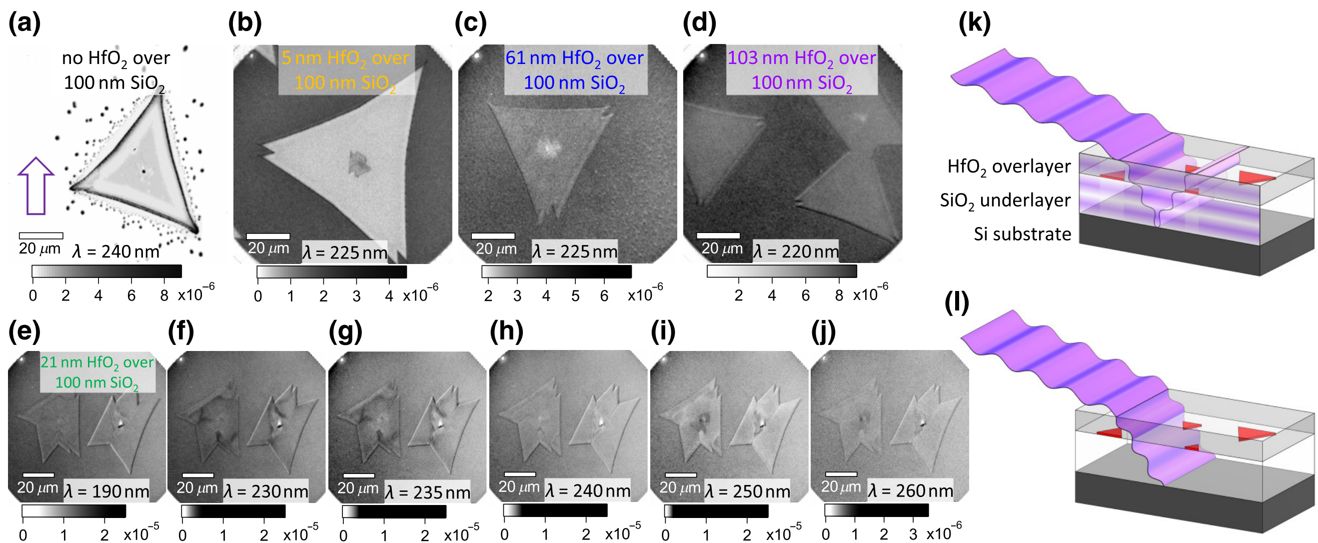

FIG. 1. PEEM images of MoS_2 flakes covered with HfO_2 films on 100-nm-thick SiO_2 underlayers, and illustrations of sample geometry and standing-wave formation within the dielectric stack. (a)–(d) show kinetic-energy-integrated photoemission yield images (i.e., the photoemission intensity is integrated across the entire electron kinetic energy range, and then converted to the unit of photoemission yield; see Ref. [40] for details). The thicknesses of HfO_2 films (0, 5, 61, and 100 nm HfO_2) are labeled at the top of image. (e)–(j) show the photon wavelength dependence of the kinetic-energy-integrated PEY images for 21-nm-thick HfO_2 overlayer. Scale bars for photoemission yield, shown at the bottom of (a)–(j), represent higher yield as dark gray. The photon wavelength used for these measurements are labeled in each image. The arrow in (a) indicates the in-plane direction of the incident wave vector of deep-UV sample illumination. Purple waves and red triangular islands in (k) and (l) depict deep-UV illumination of buried MoS_2 flakes with an incident angle of 73° off normal to the sample surface defined by the instrument's geometry. When the deep-UV wavelength matches the cavity's resonance condition, a standing wave forms in the dielectric, as illustrated by the color gradation (purple) in the dielectric films in (k). The nonresonance case is illustrated in (l).

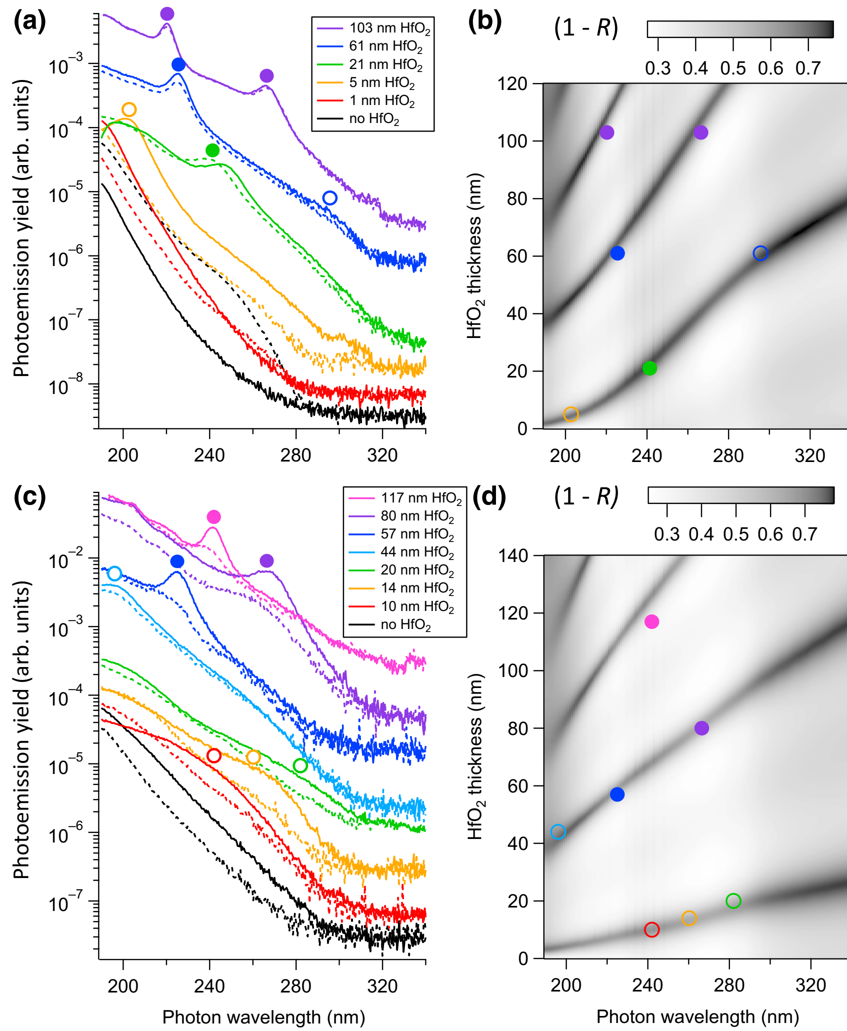

FIG. 2. Photoemission yield spectra and the modeled optical absorption of the dielectric cavity. (a) PEY spectra as a function of photon energy obtained at sample locations over MoS_2 flakes (dotted lines) and SiO_2 (solid lines), for dielectric stacks with 100-nm-thick SiO_2 and different HfO_2 overlayer thicknesses. Spectra except for black ones are shifted along the vertical axis for clarity. Filled circles indicate peak positions in PEY spectra, while open circles denote the positions of low-intensity peaks. We determine all peak positions from PEY spectra over SiO_2 (solid lines). (b) Total optical absorption $(1 - R)$ calculated for dielectric cavities comprised of stacks of HfO_2 films with varying thickness atop 100-nm-thick SiO_2. The filled and open circles overlaid on calculated absorption spectra in (b) depict the positions of resonance peaks in PEY spectra (a). (c) PEY spectra similar to (a) for dielectric stacks with nominally 12-nm-thick SiO_2 and different HfO_2 overlayer thicknesses. Again, spectra except for black ones are shifted along the vertical axis for clarity. (d) Total optical absorption $(1 - R)$ calculated for dielectric cavities comprised of stacks of HfO_2 films with varying thickness atop 15-nm-thick SiO_2.

via deep-UV photon illumination. To support this assertion, we first describe a signature of the optical standing waves by comparing the experimentally determined photoemission yield to the modeled optical absorption within the dielectric stack. We model the optical absorption using a transfer-matrix approach that captures thin-film interference. In Fig. 2(a), we show the wavelength-dependent PEY measured from samples with varying HfO_2 overlayer thicknesses atop 100-nm-thick SiO_2 underlayers. The definition of the PEY and the measurement protocol is given in Refs. [[40] and [41]], respectively. We obtain PEY spectra from a series of total photoemission yield images recorded as a function of the photoexcitation wavelength at a given sample location.

Most importantly, PEY spectra exhibited resonancelike peaks shown in Fig. 2(a), highlighted by open and filled circles. Solid lines in Fig. 2(a) represent PEY spectra obtained from the area above HfO_2-covered SiO_2 (*without* the MoS_2 flakes). Dotted lines in Fig. 2(a) are the spectra taken at sample locations over HfO_2-covered MoS_2 flakes on SiO_2. We quantify the wavelength of resonancelike peaks in Fig. 2(a), denoted by filled circles, by fitting PEY spectra with Gaussian functions superimposed over a polynomial background. Open circles designate peaks that are not clearly defined, due to relatively low signal-to-noise ratio (therefore, no fitting is conducted). Fitting of resonancelike peaks shows a slight shift in peak positions between the dotted and solid lines for samples with HfO_2 thicknesses >5 nm. We discuss the cause and implications of this slight shift in the subsequent section describing Fig. 3. Aside from these peak shifts, PEY spectra are very similar between the sample areas over MoS_2 and SiO_2. For thin HfO_2 overlayers ≤ 5 nm, Fig. 2(a) shows PEY spectra from areas above the MoS_2 flakes and the SiO_2 that are noticeably different, with peaks apparent for SiO_2 areas only. Overall, the PEY spectra exhibited a near-exponential increase for shorter photoexcitation wavelengths (i.e., higher photon energy) as reported previously [42,43], with an abrupt decrease below $\lambda = 190$ nm (not shown). This abrupt decrease of the PEY is due to reduced photon flux and hence lower photoemission intensity, owing to poor light transmission by the optics in this

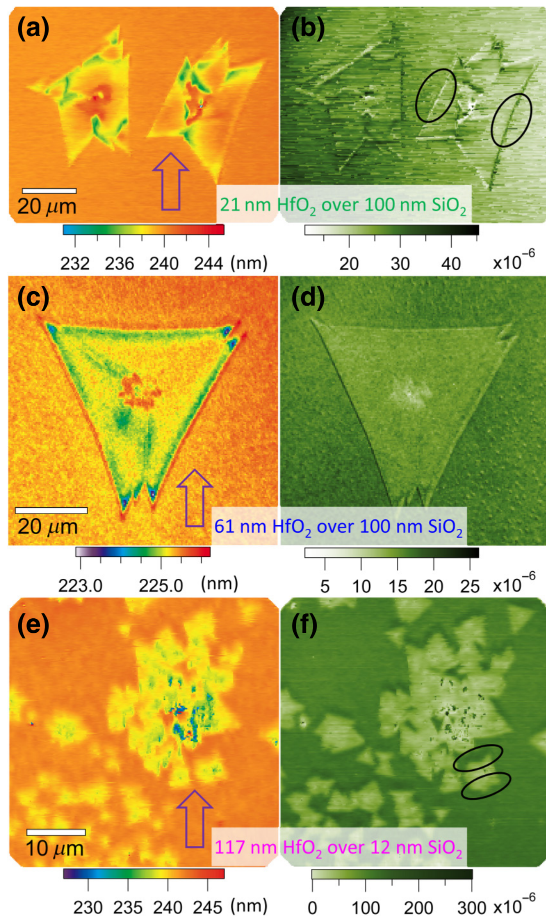

FIG. 3. Spatial mapping of cavity mode resonance peak wavelengths [(a), (c), and (e)] and total peak areas [(b), (d), and (f)] for samples with 21-nm- and 61-nm-thick HfO_2 overlayers on 100-nm-thick SiO_2, and 117-nm-thick HfO_2 overlayers on nominally 12-nm-thick SiO_2. The unit of total peak area is proportional to the wavelength times the photoemission yield. The arrows in (a), (c), and (e) indicate the in-plane direction of the incident wave vector of deep-UV sample illumination. Ovals highlight the areas with contrast asymmetries (see the main text for details).

wavelength range and the cutoff of the light source. For our setup, we also note that the measurement of light intensity for wavelengths below $\lambda = 200$ nm is less accurate than that above $\lambda = 200$ nm due to a calibration issue [40].

We establish that resonancelike peaks in PEY spectra shown in Fig. 2(a) are signatures of optical standing waves (i.e., cavity resonance of the thin-film waveguides) by comparing the peak positions to the modeled optical absorption. In Fig. 2(b), the gray-scale contrast shows the modeled total optical absorption $(1 - R)$ as a function of the photoexcitation wavelength, and HfO_2 overlayer thickness of the dielectric stacks. Higher optical absorption is represented as darker gray. We obtain the total optical absorption using the transfer-matrix method to account for light propagation and interference within an optical cavity comprised of a Si substrate, a 100-nm-thick SiO_2 underlayer, and a HfO_2 overlayer. We averaged the *s*- and *p*-polarized illuminations to simulate unpolarized light at 73° angle of incidence, consistent with the experimental geometry. Optical parameters used for the model are given in Ref. [44].

In Fig. 2(b), four high-absorption bands (i.e., darker gray bands), which extend from smaller HfO_2 thickness at lower photon wavelength to larger HfO_2 thickness at higher photon wavelength, correspond to optical absorption modes of the dielectric cavity. The positions of resonancelike peaks in PEY spectra from the HfO_2-covered SiO_2 areas without the MoS_2 flakes [circles in Figs. 2(a) and 2(b)] match remarkably well with the wavelengths of high optical absorption expected from the model [45]. This result supports the notion of higher PEY due to enhanced light absorption from the formation of optical standing waves within the dielectric stack. Figures 1(k) and 1(l) illustrate the resonance and nonresonance conditions, respectively [31]. Furthermore, the formation of optical standing waves explains the wavelength-dependent changes in image contrast observed between buried MoS_2 flakes and surrounding areas shown in Figs. 1(e)–1(j) [38]. Specifically, the image contrast increases at wavelengths near the resonancelike peaks in PEY spectra (e.g., between 230 and 250 nm for the 21-nm-thick HfO_2 film) and is less prominent at other wavelengths. At these resonance wavelengths, the presence of the MoS_2 flakes "detuned" the cavity resonance resulting in significant changes in PEY that are observed as image contrast. This "detuning" of the resonance is also the origin for the slight shift in the PEY peak shown in Fig. 2(a) between the locations over MoS_2 flakes and over the surrounding SiO_2 area.

We underscore the formation of the optical standing wave by examining PEY spectra from complementary dielectric stacks, in which the SiO_2 underlayer is nominally 12 nm thick, as opposed to 100-nm-thick SiO_2 discussed thus far. Most of the MoS_2 flakes are monolayer specimens with some coexisting multilayer areas (mostly less than five layers). The 12-nm-thick SiO_2 underlayer results inadvertently from the growth of MoS_2 flakes on Si wafers covered with native oxide. The thickness of underlayer SiO_2 was 12 nm estimated using optical ellipsometry [46].

Figure 2(c) shows PEY spectra as a function of the incident photon wavelength for samples having a thinner SiO_2 underlayer, with varying thicknesses of HfO_2 overlayers. Again, the dotted lines of Fig. 2(c) represent the PEY spectra taken at sample locations over MoS_2 flakes, whereas solid lines represent spectra over the surrounding SiO_2 areas. Similar to the dielectric stacks with 100-nm-thick SiO_2 underlayers, the PEY spectra in Fig. 2(c) exhibited near-exponential increases toward shorter photoexcitation wavelengths. Importantly, the resonancelike peaks ride atop the near-exponential trend of PEY spectra, highlighted by open and filled circles. This result substantiates the optical standing-wave formation in the dielectric

stack that is general and not limited to particular dielectric stacks. Differences do exist in the PEY spectra between films of two SiO_2 underlayer thicknesses, however. There is a lack of prominent resonant peaks for all regions in which HfO_2 overlayers are less than approximately 50 nm. Additionally, we see the suppressed intensity of resonance-like peaks for areas covered by MoS_2 flakes compared to surrounding areas [compare solid and dotted lines of Fig. 2(c)]. This observation contrasts with the dielectric stacks with thicker SiO_2 underlayers [Fig. 2(a)], where the amplitudes of the resonancelike peaks between the two regions are nearly equivalent in magnitude, albeit shifted in wavelength.

For dielectric stacks with nominally 12-nm-thick SiO_2 underlayers, we again test the formation of the optical standing wave by comparing the peak positions in the PEY spectra to the modeled optical absorption, as shown in Fig. 2(d). The high optical absorption bands represented as darker gray show remarkable coincidence to the PEY peak positions. We note that the magnitude of the modeled absorption is lower for the dielectrics stacks with the thinner SiO_2 underlayers [Fig. 2(d)] compared to those with 100-nm-thick SiO_2 underlayers [Fig. 2(b)]. The reduced absorption is most apparent in the bottom portion of Fig. 2(d) where the HfO_2 overlayer is thinnest. We postulate that this reduced absorption contributes to the lack of well-established resonance peaks observed in the PEY for sub-50-nm HfO_2 overlayers, shown in Fig. 2(c).

We obtain the best match between the modeled optical absorption and the PEY peak positions by assuming 15-nm-thick SiO_2 underlayers instead of 12 nm, the nominal thickness of SiO_2 underlayers being derived from optical ellipsometry [46]. We speculate that this discrepancy may be due to the optical properties of the SiO_2 underlayer, different from that of a pure thermal oxide, as well as defective interfaces between thin-film dielectrics and the Si substrate promoted during the ALD growth of HfO_2 overlayers. Defected SiO_2 underlayers could also explain the reduced resonance peak intensity in areas covered by MoS_2 flakes, as defects could result in the absence of a well-defined SiO_2-MoS_2 interface capable of bleeding out the optical wave, partially quenching the resonant effect [47].

Based on the examinations of two complementary dielectric stacks, we conclude that the resonancelike peaks in the PEY spectra as well as the wavelength-dependent image contrast arise due to the formation of optical standing waves from deep-UV photons used for PEEM imaging. In the UV range, the refractive indices of HfO_2 and SiO_2 are relatively high. Whereas, Si has a low refractive index particularly below the wavelength of 270 nm reaching close to unity around 200 nm. The differences in the refractive indices allow for forming dielectric cavities particularly for the photons at shorter wavelength. The effect of these standing waves, in turn, provides a means to perform subsurface PEEM imaging beneath nonconductive dielectric layers.

C. Microscopic analysis of the optical phase contrast

PEEM imaging based on deep-UV standing waves has the potential not only for subsurface imaging but also for mapping local optical parameters (i.e., the refractive index or high-frequency dielectric function), which dictate the propagation of deep-UV photons. To explain, we first recognize that the resonance of the optical cavity, and thus the PEY, is sensitive to the optical path taken by the deep-UV photons. These photons propagate based on the optical constants of the materials forming the cavity, and the wavelength and incident angle of the light [18–22]. Incorporating atomically thin MoS_2 flakes alters the propagation of the photons locally, resulting in a change of the optical cavity. This modifies the PEY spectrum's resonant wavelength and total peak area [48]. The resonance-peak wavelength and area, therefore, contain information regarding local optical properties.

Exploiting this notion and the spectroscopic imaging data, we show in Fig. 3 false color maps of the local cavity resonance peaks in terms of wavelength [3(a), 3(c), and 3(e)] and total peak area [3(b), 3(d), and 3(f)]. We obtain these false color maps for samples with 21-nm- and 61-nm-thick HfO_2 overlayers on 100-nm-thick SiO_2 underlayers, and for 117-nm-thick HfO_2 on nominally 12-nm-thick SiO_2. Using the three-dimensional dataset of the spectroscopic imaging, we create these images by fitting the PEY spectrum from each pixel in the image, whereupon we assign a color based on the value of the resonance peak wavelength or the total peak area.

The resulting images provide an impressive level of structural details for the buried MoS_2 flakes, as shown in Fig. 3. Beyond merely exhibiting the expected triangular geometry characteristic of MoS_2 flakes derived from chemical-vapor-deposition processes [49], the peak wavelength image [Fig. 3(a)] indicates that each specimen is comprised of three to four flakes that coalesce and merge during growth. Specifically, the locations of low-wavelength resonance peaks (green areas) coincide with boundaries expected to exist between domains with different crystallographic orientations. The orange to red areas, meanwhile, match the locations where multilayer MoS_2 is expected. Similarly, the total peak area map of Fig. 3(b) highlights the locations of domain boundaries as well. Unlike peak wavelength images, the left and right sides of MoS_2 flakes appear different in the peak area image in Fig. 3(b), as highlighted by ovals. We suspect this contrast asymmetry results from the incident light direction [arrow in Fig. 3(a)] and the consequent light interference as deep-UV photons propagate through areas with encapsulated MoS_2 flakes. We find similar image-contrast variation at the boundaries between flakes and multilayer areas for

the sample with the 61-nm-thick [Figs. 3(c) and 3(d)] and 103-nm-thick HfO_2 overlayers (not shown) on 100-nm-thick SiO_2 underlayer. Although less clearly resolved, the sample with 117-nm-thick HfO_2 on nominally 12-nm-thick SiO_2 underlayer also displays the triangular geometry of buried MoS_2 flakes in both resonant peak wavelength and the total peak area images [Figs. 3(e) and 3(f)], as well as contrast asymmetry highlighted by ovals in the total peak area image [Fig. 3(f)].

Spectroscopic imaging of the standing-wave resonances demonstrates its outstanding sensitivity to the structural details of the buried MoS_2 flakes, despite their few-atom thicknesses. This structural sensitivity is a consequence of optical interference phenomena, which are acutely sensitive to changes in the optical path length, even down to the thickness of a MoS_2 monolayer. Accordingly, PEEM imaging based on deep-UV photoexcitation provides high subsurface sensitivity. Functionally, the maps of resonance peak wavelength and total peak area shown in Fig. 3 are analogous to optical phase contrast images obtained with optical microscopy (i.e., Nomarski microscopy) [1,3]. However, in the present study, the electron optics of PEEM renders intrinsically high spatial resolution [16]. Quantitative evaluation based on finite-element analysis of the optical interference that results from the presence of MoS_2 flakes is a subject of future study.

D. Extensions of PEEM-based subsurface imaging

We test the general applicability of this deep-UV PEEM approach to image atomically thin MoS_2 flakes encapsulated by two other dielectrics commonly used in micro and nanoelectronics. In Figs. 4(a) and 4(b), we show subsurface images of MoS_2 flakes sandwiched between the SiO_2 underlayer and overlayers of Al_2O_3 and SiO_2, respectively. In each case, MoS_2 flakes are clearly imaged, showcasing the extended applicability of this approach to other insulating or wide-band-gap materials.

Finally, we note that the concept of subsurface microscopy using deep-UV PEEM can be further extended by incorporating table-top, coherent and incoherent light sources. Controlling the polarization of light may offer additional insight for probing buried structures and their optical properties (i.e., functional imaging [2]). Such polarization-dependent measurement as well as optical standing-wave measurement will be particularly useful when exploiting multiphoton photoemission processes [50] based on visible photoexcitation, where optical properties extracted for visible wavelengths will have broader scientific and technological impacts. We also expect that changing the energy or the incident angle of the light may enable tuning the sampling depth on the fly by shifting the region subjected to the high electromagnetic field [20,22,51]. Some of these imaging approaches are readily available for PEEM in a standard laboratory environment

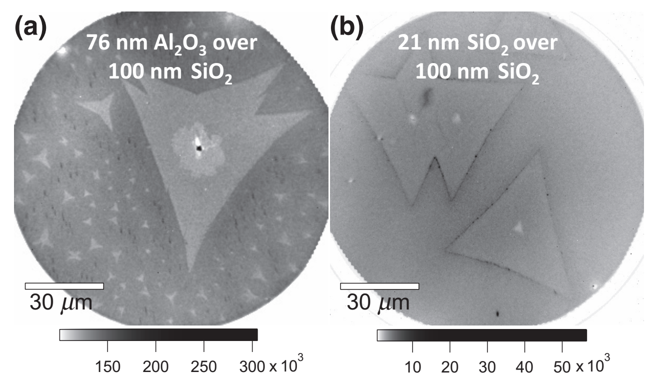

FIG. 4. PEEM images of MoS_2 flakes covered with various dielectric materials. (a) MoS_2 flakes sandwiched between 100-nm-thick SiO_2 (underlayer) and 76-nm-thick Al_2O_3 (overlayer). The cw light source is used for this measurement. See "Photoemission electron microscopy measurement" section of the Supplemental Material [35] for details. (b) MoS_2 flakes sandwiched between a 100-nm-thick SiO_2 (underlayer) and a 21-nm-thick SiO_2 (overlayer). We use the deep-UV laser light source for this measurement. The photon energy used for measurements in (a) and (b) is 5.9 eV ($\lambda = 210$ nm).

as various deep-UV light sources are emerging rapidly, with some becoming commercially available in recent years [52].

ACKNOWLEDGMENTS

We acknowledge insightful discussions with E. Bussmann, I. Ermanoski, M. B. Sinclair, and W. T. S. Luk at Sandia National Laboratories, T. Taniuchi at the University of Tokyo, and M. Donath at the University of Münster. We performed the PEEM work at the Center for Integrated Nanotechnologies (CINT), an Office of Science User Facility operated for the U.S. Department of Energy (DOE) Office of Science (DE-AC04-94AL85000). This work is supported by the CINT user program and Sandia LDRD. Sandia National Laboratories is a multimission laboratory managed and operated by National Technology and Engineering Solutions of Sandia, LLC., a wholly owned subsidiary of Honeywell International, Inc., for the U.S. Department of Energy's National Nuclear Security Administration under contract DE-NA0003525. The views expressed in the article do not necessarily represent the views of the U.S. Department of Energy or the United States Government.

[1] A. H. Landzberg, *Microelectronics Manufacturing Diagnostics Handbook* (Van Nostrand Reinhold, New York, 1993).

[2] M. Soliman, Y. Ding, and L. Tetard, Nanoscale subsurface imaging, J. Phys. Condens. Mat. **29**, 173001 (2017).

[3] S. Perkowitz, D. G. Seller, and W. M. Duncan, Optical characterization in microelectronics manufacturing, J. Res. Natl. Inst. Stand. Technol. **99**, 605 (1994).

[4] L. Reimer, *Scanning Electron Microscopy: Physics of Image Formation and Microanalysis* (Springer Series in Optical Sciences, Berlin, Heidelberg, 1985).

[5] D. B. Holt and D. C. Joy, *SEM Microcharacterization of Semiconductors* (Academic Press, Saint Louis, 1989), Vol. 12.

[6] J. Cazaux, From the physics of secondary electron emission to image contrasts in scanning electron microscopy, J. Electron Microsc. **61**, 261 (2012).

[7] H.-J. Fitting and M. Touzin, Time-dependent start-up and decay of secondary electron emission in dielectrics, J. Appl. Phys. **108**, 033711 (2010).

[8] A. M. Donald, The use of environmental scanning electron microscopy for imaging wet and insulating materials, Nat. Mat. **2**, 511 (2003).

[9] B. L. Thiel and M. Toth, Secondary electron contrast in low-vacuumâĹŢenvironmental scanning electron microscopy of dielectrics, J. Appl. Phys. **97**, 051101 (2005).

[10] C. Plassard, E. Bourillot, J. Rossignol, Y. Lacroute, E. Lepleux, L. Pacheco, and E. Lesniewska, Detection of defects buried in metallic samples by scanning microwave microscopy, Phys. Rev. B **83**, 121409(R) (2011).

[11] G. Gramse, E. Brinciotti, A. Lucibello, S. B. Patil, M. Kasper, C. Rankl, R. Giridharagopal, P. Hinterdorfer, R. Marcelli, and F. Kienberger, Quantitative sub-surface and non-contact imaging using scanning microwave microscopy, Nanotechnology **26**, 135701 (2015).

[12] L. You, J.-J. Ahn, Y. S. Obeng, and J. J. Kopanski, Subsurface imaging of metal lines embedded in a dielectric with a scanning microwave microscope, J. Phys. D Appl. Phys. **49**, 045502 (2016).

[13] J. Kirz and C. Jacobsen, The history and future of x-ray microscopy, J. Phys. Conf. Ser. **186**, 012001 (2009).

[14] H. Ade and H. Stoll, Near-edge x-ray absorption fine-structure microscopy of organic and magnetic materials, Nat. Mat. **8**, 281 (2009).

[15] S. Hufner, *Photoelectron Spectroscopy – Principles and Applications* (Springer, Berlin, Heidelberg, 2003).

[16] E. Bauer, *Surface Microscopy with Low Energy Electrons* (Springer, Berlin, Heidelberg, 2014).

[17] We define depth sensitivity as the ability to image something that is situated beneath another material. Higher depth sensitivity corresponds to the ability to image through a thicker material or overlayer.

[18] J. Maul, J. Lin, A. Oelsner, D. Valdaitsev, N. Weber, M. Escher, M. Merkel, H. Seitz, U. Heinzmann, U. Kleineberg, and G. Schönhense, Phase defect inspection of multilayer masks for 13.5 nm optical lithography using PEEM in a standing wave mode, Surf. Sci. **601**, 4758 (2007).

[19] J. Lin, N. Weber, M. Escher, J. Maul, H.-S. Han, M. Merkel, S. Wurm, G. Schönhense, and U. Kleineberg, Three-dimensional characterization of extreme ultraviolet mask blank defects by interference contrast photoemission electron microscopy, Opt. Express **16**, 15343 (2008).

[20] S.-H. Yang, A. X. Gray, A. M. Kaiser, B. S. Mun, B. C. Sell, J. B. Kortright, and C. S. Fadley, Making use of x-ray optical effects in photoelectron-, Auger electron-, and x-ray emission spectroscopies: Total reflection, standing-wave excitation, and resonant effects, J. Appl. Phys. **113**, 073513 (2013).

[21] U. Neuhäusler, A. Oelsner, J. Slieh, M. Brzeska, A. Wonisch, T. Westerwalbesloh, H. Brückl, M. Schicketanz, N. Weber, M. Escher, M. Merkel, G. Schönhense, U. Kleineberg, and U. Heinzmann, High-resolution actinic defect inspection for extreme ultraviolet lithography multilayer mask blanks by photoemission electron microscopy, Appl. Phys. Lett. **88**, 053113 (2006).

[22] A. X. Gray, Future directions in standing-wave photoemission, J. Electron Spectrosc. **195**, 399 (2014).

[23] We define low-energy photons as the UV light with the energy slightly larger than the sample's work function to promote the photoemission process. We refer medium-energy photons to extreme UV (10–121 nm, https://en.wikipedia.org/wiki/Ultraviolet) and soft x ray (150–200 nm, https://en.wikipedia.org/wiki/X-ray). Similarly, high-energy photons include x rays with energy higher than a few keV (150–200 nm, https://en.wikipedia.org/wiki/X-ray).

[24] M. P. Seah and W. A. Dench, Quantitative electron spectroscopy of surfaces: A standard data base for electron inelastic mean free paths in solids, Surf. Interface Anal. **1**, 2 (1979).

[25] S. Tanuma, C. J. Powell, and D. R. Penn, Calculations of electron inelastic mean free paths. III. Data for 15 inorganic compounds over the 50–2000 eV range, Surf. Interface Anal. **17**, 927 (1991).

[26] X. Kozina, G. H. Fecher, G. Stryganyuk, S. Ouardi, B. Balke, C. Felser, G. Schönhense, E. Ikenaga, T. Sugiyama, N. Kawamura, M. Suzuki, T. Taira, T. Uemura, M. Yamamoto, H. Sukegawa, W. Wang, K. Inomata, and K. Kobayashi, Magnetic dichroism in angle-resolved hard x-ray photoemission from buried layers, Phys. Rev. B **84**, 054449 (2011).

[27] T. Wakita, T. Taniuchi, K. Ono, M. Suzuki, N. Kawamura, M. Takagaki, H. Miyagawa, F. Guo, T. Nakamura, T. Muro, H. Akinaga, T. Yokoya, M. Oshima, and K. Kobayashi, Hard X-ray photoelectron emission microscopy as tool for studying buried layers, Jpn. J. Appl. Phys. **45**, 1886 (2006).

[28] M. Patt, C. Wiemann, N. Weber, M. Escher, A. Gloskovskii, W. Drube, M. Merkel, and C. M. Schneider, Bulk sensitive hard x-ray photoemission electron microscopy, Rev. Sci. Instrum. **85**, 113704 (2014).

[29] K. Keyshar, M. Berg, X. Zhang, R. Vajtai, G. Gupta, C. K. Chan, T. E. Beechem, P. M. Ajayan, A. D. Mohite, and T. Ohta, Experimental determination of the ionization energies of MoS_2, WS_2, and $MoSe_2$ on SiO_2 using photoemission electron microscopy, ACS Nano **11**, 8223 (2017).

[30] A. F. Zatsepin, D. Yu. Biryukov, and V. S. Kortov, Method for the analysis of nonselective spectra of optically stimulated electron emission from irradiated dielectrics, Phys. Status Solidi A **202**, 1935 (2005).

[31] H. Ade, W. Yang, S. L. English, J. Hartman, R. F. Davis, R. J. Nemanich, V. N. Litvinenko, I. V. Pinayev, Y. Wu, and J. M. J. Madey, A free electron laser-photoemission electron microscope system (FEL-PEEM), Surf. Rev. Lett. **5**, 1257 (1998).

[32] P. J. Feibelman, Film-asymmetry Effects in Resonant Photoexcitation of Plasmons, Phys. Rev. Lett. **35**, 617 (1975).

[33] J. D. Koralek, J. F. Douglas, N. C. Plumb, Z. Sun, A. V. Fedorov, M. M. Murnane, H. C. Kapteyn, S. T. Cundiff, Y. Aiura, K. Oka, H. Eisaki, and D. S. Dessau, Laser Based Angle-Resolved Photoemission, the Sudden Approximation, and Quasiparticle-Like Spectral Peaks in $Bi_2Sr_2CaCu_2O_{8+\delta}$, Phys. Rev. Lett. **96**, 017005 (2006).

[34] I. Bilgin, F. Liu, A. Vargas, A. Winchester, M. K. L. Man, M. Upmanyu, K. M. Dani, G. Gupta, S. Talapatra, A. D. Mohite, and S. Kar, Chemical vapor deposition synthesized atomically thin molybdenum disulfide with optoelectronic-grade crystalline quality, ACS Nano **9**, 8822 (2015).

[35] See Supplemental Material at http://link.aps.org/supplemental/10.1103/PhysRevApplied.12.064064 for the details of the sample preparation.

[36] D. M. Hausmann, E. Kim, J. Becker, and R. G. Gordon, Atomic layer deposition of hafnium and zirconium oxides using metal amide precursors, Chem. Mater. **14**, 4350 (2002).

[37] The conformal geometry of the HfO_2 films is verified using atomic force microscopy shown in Fig. S1 of the Supplemental Material [35]. We note that 4-nm-thick HfO_2 displayed a rougher surface (peak-to-peak roughness of approximately 2 nm). The thicknesses of HfO_2 overlayers are verified using optical ellipsometry in the wavelength range of 400 to 1200 nm.

[38] Fig. S2 shows a sequence of image contrast changes as a function of photoexcitation wavelength for the 103-nm-thick HfO_2 film on 100-nm-thick SiO_2, as well as 57-nm-thick HfO_2 and 117-nm-thick HfO_2 overlayers on nominally 12-nm-thick SiO_2. Similar image contrast appears for 61-nm-thick HfO_2 on a 100-nm-thick SiO_2 underlayer, not shown here, but quantified in Fig. 3.

[39] I. Gueye, G. Le Rhun, O. Renault, D. Cooper, D. Ceolin, J.-P. Rueff, and N. Barrett, Operando hard x-ray photoelectron spectroscopy study of the $Pt/Ru/PbZr_{0.52}Ti_{0.48}O_3$ interface, Appl. Phys. Lett. **111**, 032906 (2017).

[40] Photoemission yield is calculated by normalizing the photoemission intensity (imaging electron detector's count) by the number of photons per unit area (i.e., photon flux), based on the measurement of the light intensity using a photodiode (Thorlabs, S120VC) in air. Therefore, the measured photoemission yield is not an absolute value. The responsivity of the photodiode below $\lambda = 200$ nm is assumed to be same to that of $\lambda = 200$ nm, and not calibrated. We presume that this uncertainty of the light intensity below $\lambda = 200$ nm makes the PEY spectra less accurate in this wavelength range. See 'Photoemission electron microscopy measurement' section in the Supplemental Material for further details [35].

[41] M. Berg, K. Keyshar, I. Bilgin, F. Liu, H. Yamaguchi, R. Vajtai, C. Chan, G. Gupta, S. Kar, P. Ajayan, T. Ohta, and A. D. Mohite, Layer dependence of the electronic band alignment of few-layer MoS_2 on SiO_2 measured using photoemission electron microscopy, Phys. Rev. B **95**, 235406 (2017).

[42] J. C. McMenamin and W. E. Spicer, Photoemission studies of layered transition-metal dichalcogenides: MoS_2, Phys. Rev. B **16**, 5474 (1977).

[43] A. F. Zatsepin, V. S. Kortov, N. V. Gavrilov, and D. Y. Biryukov, Photoemission and luminescence properties of quartz glass implanted with Cu^+ ions, J. Surf. Investig. X-ray Synchrotron Neutron Tech. **2**, 450 (2008).

[44] Optical properties for HfO_2 are obtained from S. Gieraltowska, L. Wachnicki, B. S. Witkowski, R. Mroczynski, P. Dluzewski, and M. Godlewski, Characterization of dielectric layers grown at low temperature by atomic layer deposition, Thin Solid Films **577**, 97 (2015) and for SiO_2 from I. H. Malitson, Interspecimen comparison of the refractive index of fused silica, J. Opt. Soc. Am. **55**, 1205 (1965). Properties for Si, meanwhile, are acquired from E. Palik, Handbook of Optical Constants of Solids, 1998. Indices are assumed constant for the wavelength below the minimum for which they are reported.

[45] We note that the model tends to overestimate the cavity thickness or underestimate the photon energy for a given resonant wavelength, particularly for larger HfO_2 thicknesses. This general tendency may result from a slight underestimate of the optical constants used in the model, or the effect of the interface between the dielectric films and Si substrate.

[46] The 'Sample preparation' section in the Supplemental Material [35] provides more details regarding the samples with nominally 12-nm-thick SiO_2 underlayers.

[47] T. Stenmark, R. C. Word, and R. Könenkamp, Determination of the Goos-Hänchen shift in dielectric waveguides via photo emission electron microscopy in the visible spectrum, Optics Express **24**, 3839 (2016).

[48] Total peak area is the integrated intensity under the resonance peak with units proportional to the wavelength times the photoemission yield.

[49] A. M. van der Zande, P. Y. Huang, D. A. Chenet, T. C. Berkelbach, Y. You, G.-H. Lee, T. F. Heinz, D. R. Reichman, D. A. Muller, and J. C. Hone, Grains and grain boundaries in highly crystalline monolayer molybdenum disulphide, Nat. Mat. **12**, 554 (2013).

[50] G. Spektor, D. Kilbane, A. K. Mahro, B. Frank, S. Ristok, L. Gal, P. Kahl, D. Podbiel, S. Mathias, H. Giessen, F.-J. Meyer zu Heringdorf, M. Orenstein, and M. Aeschlimann, Revealing the subfemtosecond dynamics of orbital angular momentum in nanoplasmonic vortices, Science **355**, 1187 (2017).

[51] A. X. Gray, C. Papp, B. Balke, S.-H. Yang, M. Huijben, E. Rotenberg, A. Bostwick, S. Ueda, Y. Yamashita, K. Kobayashi, E. M. Gullikson, J. B. Kortright, F. M. F. de Groot, G. Rijnders, D. H. A. Blank, R. Ramesh, and C. S. Fadley, Interface properties of magnetic tunnel junction $La_{0.7}Sr_{0.3}MnO_3/SrTiO_3$ superlattices studied by standing-wave excited photoemission spectroscopy, Phys. Rev. B **82**, 205116 (2010).

[52] T. Taniuchi, Y. Kotani, and S. Shin, Ultrahigh-spatial-resolution chemical and magnetic imaging by laser-based photoemission electron microscopy, Rev. Sci. Instrum. **86**, 023701 (2015).